

Spectroscopic Gravitational Lensing and Limits on the Dark Matter Substructure in Q2237+0305

R. Benton Metcalf¹

Department of Astronomy and Astrophysics, University of California, Santa Cruz, CA 95064 USA

and

Leonidas A. Moustakas

Space Telescope Science Institute, 3700 San Martin Drive, Baltimore, MD 21218 USA

and

Andrew J. Bunker

Institute of Astronomy, Cambridge University, Madingley Road, CB3 0HA United Kingdom

and

Ian R. Parry

Institute of Astronomy, Cambridge University, Madingley Road, CB3 0HA United Kingdom

ABSTRACT

Spatially resolved spectroscopic data from the CIRPASS integral field unit (IFU) on Gemini are used to measure the gravitational lensing of the 4-image quasar Q2237+0305 on different size scales. A method for measuring the substructure present in the lens using observations at multiple wavelengths is demonstrated to be very effective and independent of many of the degeneracies inherent in previous methods. The magnification ratios of the QSO's narrow line region (NLR) and broad line region (BLR) are measured and found to disagree with each other and with the published radio and mid-infrared magnification ratios. The disagreement between the BLR ratios and the radio/mid-infrared ratios is interpreted as microlensing by stars in the lens galaxy of the BLR. This implies that the mid-infrared emission region is larger than the BLR and the BLR is $\lesssim 0.1$ pc in size. We find a small difference in the shape of the H β line in image A when compared to the other images. We consider this difference too small and symmetric to be considered strong evidence for rotation or large scale infall in the H β emission region. The disagreement between the radio/mid-infrared ratios and the NLR ratios is interpreted as a signature of substructure on a larger scale, possibly the missing small scale structure predicted by the standard cold dark matter (CDM) model. Extensive lensing simulations are performed to obtain a lower limit on the amount of substructure that is required to cause this discrepancy as a function of its mass and the radial profile of the host lens. The substructure surface density is degenerate with the radial profile of the host lens, but if the expectations of the CDM model are taken into account certain radial profiles and substructure surface densities can be ruled out. A substructure mass scale as large as $10^8 M_{\odot}$ is strongly disfavored while $10^4 M_{\odot}$ is too small if the radio and mid-infrared emission regions have the expected sizes of ~ 10 pc. The standard elliptical isothermal lens mass profile is not compatible with a substructure surface density of $\Sigma_{\text{sub}} < 280 M_{\odot} \text{ pc}^{-2}$ at the 95% confidence level. This is

¹Hubble Fellow

4 – 7% of the galaxy’s surface density (depending on which image position is used to evaluate this). The required substructure surface density at the required mass scale is high in comparison with the present expectations within the CDM model. Lens mass profiles that are flatter than isothermal – where the surface density in dark matter is higher at the image positions – are compatible with smaller quantities of substructure.

1. Introduction

In this paper we present observations of the lensed quasi-stellar object (QSO) Q2237+0305 and use them to address fundamental questions concerning the Cold Dark Matter (CDM) cosmological model and in addition to investigate the internal structure of the QSO. The CDM cosmological model has recently experienced great successes in predicting the distribution of galaxies and the fluctuations in the cosmic microwave background. However, there remain some challenges to this model on the scale of galaxies themselves. Simulations of structure formation within this model predict that a high level of substructure will survive tidal disruption within the large dark matter (DM) halos that surround galaxies. N-body simulations indicate that there should be plentiful subhalos in a L_* galaxy’s halo, with masses above $10^7 M_\odot$ – smaller mass scales are presently inaccessible due to limitations in resolution. If these subhalos contained stars, there would be significantly more dwarf galaxies in the Local Group than are seen (Moore et al. 1999; Klypin et al. 2001).

Various solutions to this “dwarf satellite problem” have been proposed. In particular, if the dark matter is warm (WDM) rather than cold then the small scale structure is reduced while the large scale (successful) properties of the standard paradigm are preserved. Another explanation for the absence of observable substructure is that the star formation in these small DM halos was inhibited by ionizing radiation at an early stage in the universe (e.g. Somerville (2002); Bullock, Kravtsov, & Weinberg (2000); Dong, Murray, & Lin (2003)). In this case the substructure does exist, but is invisible. Metcalf & Madau (2001) showed that this substructure could be detected in gravitational lenses. There is already some evidence in support of the need for substructure to explain the relative magnifications in strong lenses; disentangling its signature from other (also interesting) effects is the goal of this paper.

The extraction of useful information from QSO lens systems has long been hampered by uncertainties and ambiguities related to modeling the lens’ mass distribution. This has been the case for estimates of the Hubble parameter from lensing and it has necessitated long term monitoring in the optical to detect microlensing. Recently it has become an important issue in testing the CDM cosmological model by detecting the dark substructure predicted in this model. From the positions of the images and lens galaxy of a 4-image lens system, a parametric smooth mass model for the lensing galaxy and halo can be computed (including external shear), along with predictions for the three independent flux ratios. Measuring deviations between the predictions and the (differential-reddening-corrected) observed fluxes in real lenses has been used to argue that substructure is present in almost all QSO lens systems (Metcalf & Madau 2001; Chiba 2002; Metcalf & Zhao 2002; Dalal & Kochanek 2002). Some substructure has long been considered a possible explanation for inconsistencies in the observed flux ratio of B1422+231. Mao & Schneider (1998) argued that in this case the source quasar is near a cusp caustic in the lensing map and because of this the sum of the magnifications of the three closest images should be close to zero for any smooth lens model. B1422+231 and all other known cusp caustic lenses violate this relation. It is unclear how far this argument can be taken since the proximity of the

source to the caustic depends on the lens model itself (see Gaudi & Petters 2002) and stellar disks may cause the relation to be violated even very close to the cusp (Bradač et al. 2003). It is also unclear what mass or size the substructure needs to be for this argument to break down, i.e. how to measure properties of the substructure from violations of these relations. In any case, most lens systems do not have such advantageously located source quasars and the predicted flux ratios can be strongly dependent on the parametric lens models used while the image positions are degenerate. Any estimate of the mass fraction in substructure that uses a simple lens model e.g. Dalal & Kochanek (2002) is highly suspect. The observational technique used here largely avoids this important problem, as well as the problems of intrinsic variability (on the timescale of the typical time-delay between images), differential extinction, scattering in the radio and microlensing by stars in the lens galaxy.

The 4-image gravitational lens Q2237+0305, also known as Huchra’s lens after its discoverer (Huchra et al. 1985), has been a testbed for studying microlensing for many years. The QSO at redshift $z = 1.69$ is lensed by a single spiral galaxy at $z = 0.03$ which makes it especially advantageous for this. The microlensing of a QSO was first observed by Irwin et al. (1989) in this system and since then it has been extensively monitored in the optical (Woźniak et al. 2000). Q2237+0305 has also been instrumental in studying the structure of the QSO itself. Constraints on both the size of the optical emission region (Yonehara 2001; Wyithe et al. 2000b) and the mid-infrared emission region (Wyithe, Agol, & Fluke 2002) have been established through microlensing. In this paper critical measurements of the $H\beta$ broad line and [O III] narrow line ratios are added to the existing information on this lens which allows us to draw conclusions about the size of the broad line emission region (BLR) and the size of structures in the lens.

In what follows, if it is not otherwise explicitly stated, the cosmological model is taken to be a flat one with a cosmological constant of $\Omega_\Lambda = 0.7$ and a Hubble parameter of $H_o = 70 \text{ km s}^{-1} \text{ Mpc}^{-1}$. The lensing results are often expressed in term of the critical surface density defined as $\Sigma_{\text{crit}}^{-1}(z_s, z_l) = 4\pi G D_l D_{ls} / D_s$ where D_s is the angular size distance to the source, D_l is the distance to the lens and D_{ls} the distance between the lens and the source. For the case of Q2237+0305 $\Sigma_{\text{crit}} = 9.8 \times 10^3 \text{ M}_\odot \text{ pc}^{-2}$ in the above cosmology. The surface density in units of the critical density is denoted κ .

In the next Section the general method of spectroscopic gravitational lensing and its special advantages are outlined. In Section 3 the data reduction is described. The measurements of line strengths and magnification ratios are described in Section 4 along with their comparison with previously published measurements in other wavelengths. These measurements are interpreted in Section 6 in terms of the structures that could be responsible for them. A summary and discussion are given in Section 7.

2. The Method of Spectroscopic Compound Lensing

To remove much of the lens model ambiguities, a different method for detecting substructure lensing was proposed by Moustakas & Metcalf (2003) which avoids the problems arising from degeneracies in lens models, differential reddening in the optical images and scattering in the radio. This method utilizes the prediction that different emission regions of the QSO differ in size and thus should be magnified to differing degrees if substructure on a small scale is present. Comparing the magnification ratios in different wavelengths provides information on the structure of the QSO and the small scale structure of the lens that is independent of the large scale structure of the lens galaxy and halo. To describe this method we will first briefly

review what is known about the anatomy of a QSO.

2.1. sketch of QSO anatomy

The variability timescales of different spectroscopic features, and the time delays between them, have been used to establish the size and structure of different emission regions within the unified model for active galactic nuclei (AGN) and QSOs (c.f. Antonucci 1993). The basic picture consists of a supermassive black hole ($M_{bh} > 10^6 M_{\odot}$) in the core, surrounded by an accretion disk, which produces the nearly flat-spectrum continuum light. The continuum flux varies on very short timescales, less than a day, and so must be very compact (around 100 AU or $\sim 5 \times 10^{-4}$ pc). It is also known to be microlensed in the case of Q2237+0305 which puts an upper limit of 2,000 AU on its size (Yonehara 2001; Wyithe, Webster, & Turner 2000a; Wambsganss, Schneider, & Paczynski 1990). Beyond that, there are permitted lines such as the Balmer-series lines that are very broad ($v_{FWHM} > 10^3 \text{ km s}^{-1}$) due to gravitationally-induced motions. The characteristic size of this broad line region (BLR) apparently scales with the intrinsic luminosity of the host QSO (and therefore with the mass of the central black hole; Kaspi et al. 2000; Wandel 1999), such that in luminous QSOs (as opposed to, e.g., Seyfert 1's), the size of the BLR is on the order of six light-months (or ~ 0.1 pc). According to long-term studies of QSOs, the typical (rest-frame) flux variations in the QSO continuum are on the order of 10–70% (though occasional fluctuations as high as $\sim 50\times$ are possible; Ulrich, Maraschi, & Urry 1997), while the BLR variations are smaller by a factor of 2–4 (Maoz et al. 1994).

The narrow emission lines (e.g. [O III] $\lambda\lambda 4959, 5007$) do not vary in flux significantly over the time span of several years (Kaspi et al. 1996). For this reason, they have been used for calibration in long-term spectroscopic monitoring observations of low redshift QSOs for reverberation mapping experiments, by which the time delays between features of different ionization states may in principle be used to map all the components that make up QSOs (Peterson 1993). Photo-ionization arguments and cases where the narrow line region (NLR) is imaged directly, indicate that the size of the NLR extends out to 100-1000 pc and is approximately proportional to the square root of the luminosity in narrow lines.

A QSOs thermal emission in the mid-infrared is believed to come from a dusty torus that extends from a few parsecs to tens of parsecs. This belief largely comes from modeling the radiation transfer (for example Andreani, Franceschini, & Granato 1999) although recently a more direct lower limit on the size of this emission region has been made by comparing the microlensing of the optical continuum emission and the mid-IR (Wyithe et al. 2002).

A quasar can emit in the radio on a large range of size scales. The central region of a radio loud QSO is usually resolved by VLBI (very long baseline interferometry) into a core and jet, or a core and lobes on a scale of ~ 10 pc. The size of the core is limited from below by the Compton surface brightness limit which is generally in the $10 \mu\text{ac}$ range.

2.2. the differential magnification ratio (DMR)

Simulations show that if a few percent of the lens surface density is contained in substructures of mass $\sim 10^7 M_{\odot}$ then deviations of ~ 0.1 mag between the magnifications of the NLR and the BLR will be commonplace (Moustakas & Metcalf 2003). In addition, for the case of Q2237+0305 the microlensing scale or Einstein radius for ordinary stars is particularly large so if the BLR is small it could be microlensed. Our goal here has been to measure the NLR and BLR ratios in

lens Q2237+0305 and determine if substructure is evident.

To quantify our results we define the differential magnification ratio (DMR)

$$\text{DMR}^{AB} \equiv \frac{\mu_{NL}^A \mu_{BL}^B}{\mu_{BL}^A \mu_{NL}^B} = \frac{f_{NL}^A f_{BL}^B}{f_{BL}^A f_{NL}^B}. \quad (1)$$

where superscripts denote the image and subscripts the QSO emission region. The magnification is μ and the observed flux is f . Note that the DMR is independent of the intrinsic QSO luminosity, the intrinsic NLR/BLR ratio and if the NL and the BL used are close enough in wavelength it will be essentially independent of extinction. In addition, we will define the quantity $\Delta_{NL/BL} \equiv -2.5 \log(\mu_{BLR}/\mu_{NLR})$ so that $\Delta_{NL/BL}^A - \Delta_{NL/BL}^B$ is a measure of the DMR in magnitudes. If there is no substructure all three independent DMRs in a 4-image lens should be close to one (a small deviation from one is possible because of the host galaxy’s influence on the NLR; see Section 6.2). More generally the DMR can be used to compare any two measurements of the magnification ratios to see how well they agree.

3. Data Reduction

The J -band ($\lambda_c \sim 1.25 \mu\text{m}$) spectroscopy of Q2237+0305 was performed with the Cambridge Infrared Panoramic Survey Spectrograph CIRPASS Parry et al. (2000) at the f/16 focus on the 8-m Gemini-South telescope, at Cerro Pachon in Chile. CIRPASS is a near-infrared fiber-fed spectrograph, connected to a 490 element integral field unit (IFU). The variable lenslet scale was set to $0''.36$ diameter, and the hexagonal lenslets are arranged in the IFU to survey an approximately rectangular area of $13''.0 \times 4''.7$. The detectors is a $1\text{k} \times 1\text{k}$ Hawaii-I HgCdTe Rockwell array. CIRPASS can operate in the range $0.9 - 1.8 \mu\text{m}$, and a $4001/\text{mm}$ grating was used which produced a dispersion of $2.25 \text{ \AA}/\text{pix}$. The grating was tilted to place the wavelength range $\lambda\lambda 11300 - 13600 \text{ \AA}$ on the detector, covering most of the J -band transmission window out to the atmospheric absorption between the J - and H -bands. A filter at $1.67 \mu\text{m}$ blocked out redder wavelengths to reduce the dominant near-infrared background contribution. The detector pixels do not quite critically sample the spectral resolution (unresolved sky lines have $\text{FWHM}=1.7 \text{ pix}$), and the resolving power is $\lambda / \Delta\lambda_{\text{FWHM}} = 3500$.

The observations were made on the night of UT 2002 August 10 during the Director’s discretionary time instrument commissioning/IFU-demonstration science on Gemini-South. The observations spanned the airmass range $1.2 - 1.8$. A total of 3 hours integration was obtained, split into individual integrations of 30 min per pointing, although the array was read non-destructively every 10 min (i.e., 4 times per pointing, including an initial read of the bias level). Each of these ‘loops’ comprised 10 multiple reads of the detector, which were averaged to reduce the readout noise ($30e^-$ per read) by $\sqrt{10}$. These averages of each loop were subtracted from the average of the next loop of non-destructive reads, to form 3 sub-integrations of 10 min at the same telescope pointing. Comparison of these sub-integrations enabled cosmic ray strikes to be flagged, and a combined frame of 30 min was produced by summing the three sub-integrations, while masking pixels affected by cosmic rays. The seeing was $\approx 1''.0$ FWHM, and the long axis of the IFU was set to 130 deg East of North. Windshake affected the guiding, and 2 loops were lost through severe trailing of the images. These were removed from the subsequent data reduction, so the final science integration was 160 min. In total, six overlapping pointings were surveyed, each covering all of the Einstein cross: positions were not repeated to improve background subtraction and reduce the impact of bad pixels. We ‘nodded’ the target

from the top (A) to the bottom (B) of the IFU every 1800s, and introduced a small sub-dither of 2 lenslets between integrations. An initial subtraction of sky and dark current was performed using this beam-switching: for each exposure at location A , the average of the three spectra taken at B was subtracted, and vice versa. There was no overlap of the extended emission from the Einstein cross between positions A and B (a chop of $\approx 8''$). Known bad pixels were also interpolated over at this stage.

The 490 fibers span the 1k detector, with 2 pixels per fiber. A lamp was used to illuminate 10 calibration fibers immediately before the observations, in order to accurately determine the position of the fibers on the array and to focus the spectrograph at the desired wavelength range. There is significant cross-talk between adjacent fibers and we use an optimal-extraction routine² (Johnson et al. 2003) to determine the spectrum of each fiber, for each pixel on the array solving the contribution of flux from adjacent fibers (knowing their relative positions).

Immediately after the science integrations, spectral flat fields were obtained (exposures of the illuminated dome), and these were also optimally-extracted and their average flux normalized to unity. The extracted science data was then flat-fielded through division by the extracted normalized dome lamp spectra, calibrating the response of each individual fiber.

Wavelength calibration was achieved with an Argon arc lamp observed following the science exposures. Again, the individual fiber spectra were optimally extracted, and for each fiber a cubic fit was performed to the centroids of 40 arc lines, leaving *rms* residuals of 0.2 \AA . The 490 fiber spectra stacked on the slit were rectified (mapped to the same wavelength) with a 5th order polynomial transformation in x and y . This transformation was applied to the beam-switched, extracted, flat-fielded science frames. A higher-order background subtraction was then applied to this rectified data, to remove sky residuals from the beam switching caused by variation in the OH-line intensity.

The rectified, background-subtracted 2D spectra (with the dimension of wavelength and fiber number along the slit) were then converted to 3D data cubes, arranging the fibers into their physical positions in 2D on the sky, with wavelength being the third dimension. Because of the hexagonal close packing arrangement of the lenslets, alternate rows are offset by half a lens: in making the cubes this was accounted for by regridding each lenslet by two in the spatial dimensions (i.e. each lenslet is 2×2 sub-pixels of diameter $0''.18$). These six data cubes (from the six pointings of the telescope) were registered, shifting them spatially to the same location on the sky, and combined with a percentile clipping algorithm, rejecting bad pixels and residuals from cosmic ray strikes discrepant by more than 3σ .

Flux calibration was obtained through observations of the standard star HIP036096 ($V = 8.89 \text{ mag}$, type B2V), taken on the same night at similar airmass. The standard star spectrum was reduced in the same way as the science data, and the total flux found by summing 4×4 lenslets (1.5 arcsec diameter). Normalizing through division by this spectrum corrected for the severe atmospheric absorption at $> 1.33 \mu\text{m}$. The total effective throughput was determined to be ~ 8 per cent on the sky for the middle of the J -band.

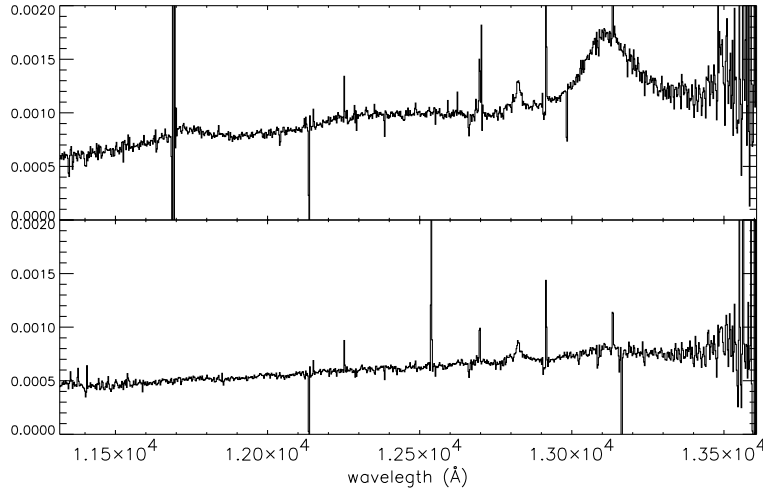


Fig. 1.— The full CIRPASS spectrum at the center of QSO image A (above) and at the center of the lens galaxy (below). The broad $H\beta$ line at 13097 \AA is clear in the QSO spectrum and in the galaxy spectrum there is only a hint of it. It is also clear that the continuum is steeper in the QSO and the Fe II “bulge” is apparent in the QSO spectrum near 12300 \AA . The prominent line at $1.28 \mu\text{m}$ is $\text{Pa}\beta$ from the calibration star.

4. Data Analysis

4.1. line strengths

To extract the line fluxes we fit a local continuum spectrum plus lines to each “spixel” in the image (i.e. the spectrum from each fiber corresponding to a unique spatial position). Example spectra from two spixels are shown in Figure 1. We are interested in the relative integrated flux within a line which should not depend critically on modeling the line shapes in detail. (In fact it is possible that microlensing might affect the line profile in detail without greatly affecting the total flux in the line in which case a fit to a smoother line profile would be preferable. See Section 6.1.1.) We start by fitting a local continuum that is linear in wavelength and a simple first order Edgeworth expansion³ to the $H\beta$ line in the nine spixels around image A, the brightest image. This fit is done only in the range $12658\text{--}13424 \text{ \AA}$ ($4706\text{--}4990 \text{ \AA}$ in QSO rest frame) to avoid the Fe II complex as much as possible. The shape of the $H\beta$ line in image A is then used as a template for all the other spixels. The spectrum at each spixel in the array is fit to a continuum level and slope along with a line strength. The result is displayed in Figure 3. In fitting the line and continuum several sky lines are masked out and along with the calibration star’s $\text{Pa}\beta$ at 12820\AA , see Figure 1. The shape and level of the Fe II complex varies greatly between QSOs and is thus very difficult to subtract (see Boroson & Green 1992). In all cases however Fe II contributes very little to the flux between 12658 \AA and the $H\beta$ line. There are three broad Fe II lines blueward of $H\beta$ at $\lambda\lambda 4924, 5018, 5169 \text{ \AA}$ which are not identified in our

²The CIRPASS data reduction software is available from <http://www.ast.cam.ac.uk/~optics/cirpass/docs.html>

³The Edgeworth expansion is a generalization of the Gaussian distribution where each addition term effects a higher moment of the distribution. The first order expansion has a skew.

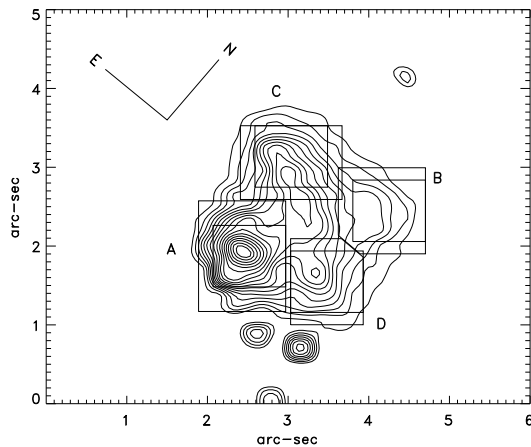


Fig. 2.— Map of the integrated flux between 11305.1 \AA and 13613.7 \AA (or 4203 \AA to 5061 \AA in the QSO’s rest-frame). The image is in the CIRPASS spixel coordinates which are rotated clockwise 50° from δ -R.A. coordinates. The squares mark the apertures used to measure the QSO fluxes as discussed in § 4.2. The conventional image labels are shown next to each aperture. Note that image B (the right most) is not prominent above the lens galaxy. The pixels are $0.18''$ in the horizontal direction and $0.156''$ in the vertical (the difference is due to the hexagonal packing of the CIRPASS lenslets). The two spots below the central image are caused by cosmic rays.

spectra. The 4924 \AA line could conceivably cause us to overestimate the slope of the continuum and underestimate the strength of $H\beta$. We can estimate the maximum effect this could have by noting that the height of this line is always below the height of the $\lambda\lambda 4450 - 4700 \text{ Fe II}$ bulge which we can measure. This contribution to the $H\beta$ strength is rather small. We include it in the $H\beta$ flux errors instead of attempting to subtract it.

The full-width-half-maxima (FWHM) of the $H\beta$ lines are 4100, 3500, 3600 and $3600 \pm 100 \text{ km s}^{-1}$ for images A, B, C and D respectively - all consistent with each other except image A. The skewnesses of the images are all small and consistent with each other. There is further discussion of the change in the shape of the $H\beta$ between images in Section 6.1.1.

The sky absorption near the 5007 \AA and 4959 \AA [O III] lines is large and sky line subtraction makes any fitting difficult. The 4959 \AA line is not detected anywhere in the field possibly because of confusion with the $\text{Fe II } \lambda 4924$ line. The 5007 \AA line is very close to a subtracted sky line to its redward side, and to its blueward the noise introduced by flux calibration and high sky absorption is too large to accurately fit a continuum. To avoid these difficulties we fit the continuum in the range $13278 - 13469 \text{ \AA}$ (independently of the continuum used in the $H\beta$ fit) then subtract this from the sum of the flux in 7 pixels (in wavelength) on top of the line (rest frame $5006 - 5010 \text{ \AA}$). This avoids the sky line. No fitting of the line shape is done.

The maps of line strengths in Figure 3 show the four QSO images distinctly and residual flux from the lens galaxy is at a low level although there are bridges between 3 of the images in [O III] at a level of 25% of the maximum. These connections go through the center of the lens galaxy and no arc connecting images is detected. The [O III] NLR is consistent with being point-like at our resolution, $\sim 0.6''$ in contrast to the $\text{C III } \lambda 1909$ NLR observed by Mediavilla et al. (1998) which shows an arc connecting images A, D and B.

To evaluate the statistical errors in our line strengths we take the part of the IFU field that is well away from the lens system where we expect no line emission and go through the

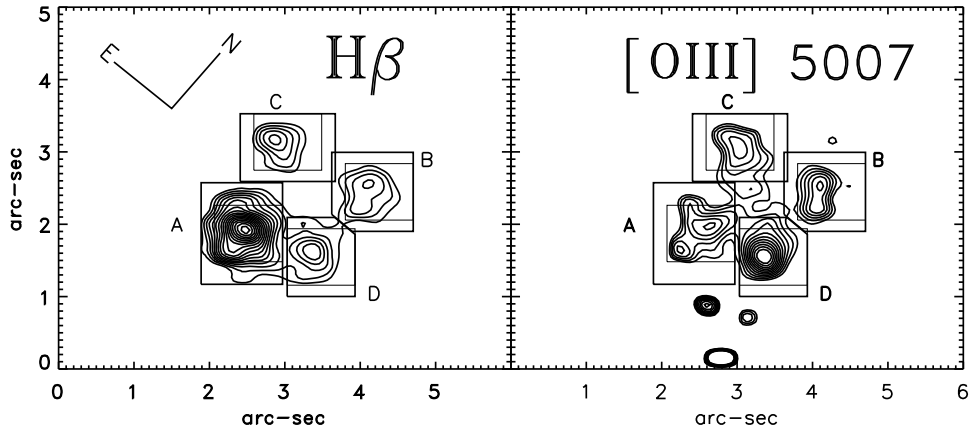


Fig. 3.— A map of $H\beta$ and $[OIII] 5007$ at the redshift of the QSO with the continuum subtracted spixel-by-spixel. The four QSO images are more distinct than in the total flux, Figure 2. Image B is clearly apparent here and the lens galaxy is not.

same continuum and line fitting procedure. We find that the average line strengths in 1036 such spixels is consistent with zero showing that there is no significant bias in our line fitting algorithm. The variance in the line strengths among these spixels is used as the statistical noise. There should be no significant signal-dependent noise since the data is dark current limited.

4.2. measuring magnification ratios

To find the total flux within a line coming from an image we must choose an aperture around each image. We use two choices for apertures. First we use square boxes five half-lenses wide ($0.90'' \times 0.78''$) centered on the QSO image positions. This is close to the expected size of the PSF. The peak in the emission is found to be the center of image A and the other image positions are set using the high precision HST relative image positions (Kochanek et al. 2000). These are shown in Figures 2 and 3. To make certain that we are capturing all the flux from each image we also extend the apertures as shown in the figures. The differential magnifications are given in Table 1 along with the separate NLR and BLR flux ratios. The errors given are the statistical errors discussed above. There is little change to the DMRs when the apertures are extended further without overlapping each other signifying that leakage of flux outside of the apertures is not significant.

Because the DMRs depend on which image is chosen to normalize them the important features to look for are the spread in the DMRs, how consistent they are with each other, and whether there is one outlier indicating that one particular image is being effected. The normalizing image's $DMR - \Delta = 0$ – should be included in this comparison. In table 1 image A is used to normalize the DMRs. For the other images the DMRs are negative and inconsistent with zero, but they are roughly consistent with each other. This indicates that the BLR in image A is anomalously bright. The simple magnification ratios in the BLR and those in NLR are also consistent with each other except those including image A which indicates that the differential extinction is not large.

	Image	B/A	C/A	D/A
small apertures	$\Delta_{\text{NL/BL}}$	-0.82 ± 0.06	-0.89 ± 0.06	-0.93 ± 0.05
	Δ_{NL}	-0.23 ± 0.06	-0.14 ± 0.06	0.09 ± 0.05
	Δ_{BL}	-1.06 ± 0.02	-1.03 ± 0.02	-0.84 ± 0.01
extended apertures	$\Delta_{\text{NL/BL}}$	-0.74 ± 0.05	-0.87 ± 0.05	-0.81 ± 0.05
	Δ_{NL}	-0.31 ± 0.05	-0.23 ± 0.04	-0.21 ± 0.04
	Δ_{BL}	-1.05 ± 0.02	-1.11 ± 0.02	-1.02 ± 0.01

Table 1: **Differential Magnification Ratios and Magnification ratios in magnitudes:** These are normalized so that $\Delta_{\text{NL/BL}}^A = 0$. Negative values indicate that image A is brighter in the simple ratios and that the BLR of image A is brighter in the DMRs.

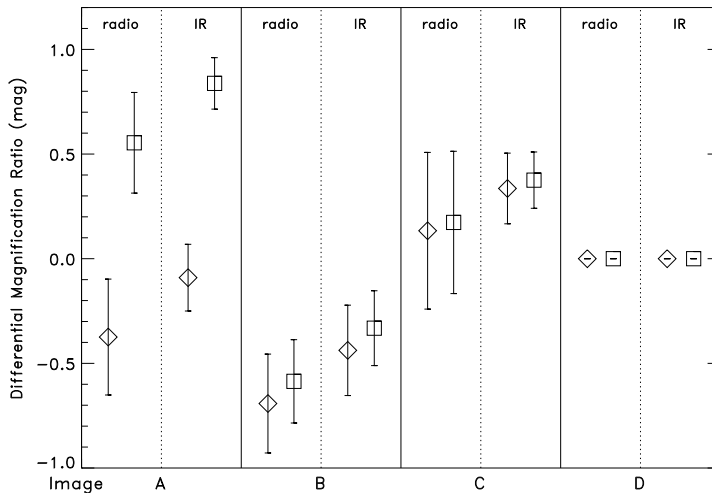


Fig. 4.— Here are the DMR with respect to the radio and mid-IR fluxes normalized to image D. The NLR DMRs (i.e. $\Delta_{\text{NL}/\text{radio}}^i - \Delta_{\text{NL}/\text{radio}}^D$ and $\Delta_{\text{NL}/\text{IR}}^i - \Delta_{\text{NL}/\text{IR}}^D$) are marked by diamonds and the BLR DMRs by squares. The radio is at 3.6 cm and the mid-IR is a combination of 8.9 μm and 11.7 μm observations. The published 1- σ error bars are shown.

4.3. Continuum

It would be useful to compare the BLR and NLR fluxes with the continuum in our data. Extracting the QSO continuum flux requires subtracting the lens galaxy contribution and all the contributions from lines. An attempt was made to model the HST NICMOS image of the lens galaxy and degrade it to the PSF of the Gemini/CIRPASS data. We concluded that because of wind-shake, the PSF of our data was not well enough characterized to accomplish this to the accuracy we would like for this paper.

5. comparison with radio and mid-infrared ratios

Two of the goals of this work are to eliminate the uncertainty inherent in radio flux ratios due to scattering by ionized gas and to eliminate differential extinction uncertainties inherent in optical or near infrared observations. However, it will be shown that in this case these effects are

image	narrow line region			broad line region		
	B/A	C/A	D/A	B/A	C/A	D/A
mid-IR/radio	-0.42 ± 0.11	0.35 ± 0.15	-0.16 ± 0.15	-1.16 ± 0.10	-0.53 ± 0.15	-0.97 ± 0.14

Table 2: The differential magnification ratios comparing the combined radio and mid-IR magnification ratio measurements to the NLR and BLR measurements. This is $\Delta_{\text{radio,mid-IR}} - \Delta_{\text{NL}}$ and $\Delta_{\text{radio,mid-IR}} - \Delta_{\text{BL}}$. The NLR and BLR errors are not doubled here. The NLR B to A and C to A DMRs disagree by 0.77 mag.

small. To do this and gain more information about substructure in the lens we construct DMRs by combining other observations with the NLR and BLR measurements. Since the sizes of the radio and mid-infrared emission regions are believed to be intermediate to those of the BLR and NLR this can give us additional information about the structure causing the anomalous DMR at the expense of these additional uncertainties.

The radio fluxes in Q2237+0305 have been measured using VLA (Very Large Array) by Falco et al. (1996) at 3.6 cm, and Agol, Jones, & Blaes (2000) have observed it in the mid-infrared, 8.9 μm and 11.7 μm . Figure 4 shows the DMRs with respect to the radio and mid-IR measurements for both the NLR and the BLR. The uncertainties in these measurements are considerably larger than those in our line measurements, but important conclusions can be drawn from them. The BLR in image A is anomalously bright with respect to the other measurements while the NLR in image A is consistent with being magnified to the same extent as both the radio and mid-IR. The consistence in the mid-IR and radio ratios is further demonstrated in the left panel of Figure 5. This suggests that the radio and the mid-IR emission regions are being lensed by the same structure and thus are similar in size which is in agreement with theoretical expectations, but, to our knowledge, has never been measured directly. It is also seen in Figure 4 and more clearly in the right panel of Figure 5 that both the radio and the mid-IR do not agree with the NLR – the image B NLR is relatively dim and the image C NLR is relatively bright. The difference between the largest DMR and the smallest DMR, the spread, is 0.77 mag. There is no clear outlier in the DMRs suggesting that the spread is not the result of an anomaly in a single image. Table 2 lists the DMRs comparing the combined radio/mid-IR with the NLR and BLR data.

The differential colors for the images of Q2237+0305 are in order $\Delta E(B - V) = -0.10 \pm 0.03$, -0.17 ± 0.03 , 0.01 ± 0.03 and 0 (Falco et al. 1999). This implies that extinction would make the NLR in image B relatively dimmer than the others which is the opposite of what is found. Also, the expected magnitude of the extinction is relatively small in comparison to the DMRs observed – $A(1.3\mu\text{m})/E(B - V) = 0.75$ mag for the Milky Way giving a change in the DMR between images A and B of 0.05 mag. This does not exclude the possibility that the extinction is very patchy so that the continuum extinction is not appropriate for the NLR, but the small differences between the colors of the images argue against this being a large effect.

The simplest interpretation of the anomalous DMRs in Figure 5 is that the mid-IR and radio emission regions are larger than the BLR and whatever is causing the extra magnification of the BLR in image A is too small to significantly change the magnification of the mid-IR, radio or NLR. Then there is some larger structures that are causing the NLR ratios to be incompatible with the mid-IR and radio ratios.

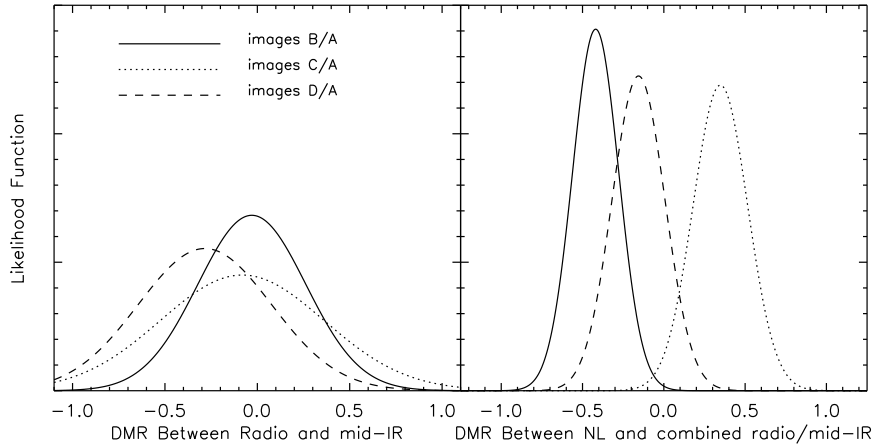


Fig. 5.— The likelihood functions for differential magnification ratios. In the left panel is the DMR between the mid-IR and radio ratios with respect to image A (DMR=0 means the ratio of mid-IR to radio is the same as in image A) using the published errors. All three DMRs are compatible with zero. In the right panel it is assumed that the magnification ratios in mid-IR and radio are the same and they combined into one set of measurements. The likelihood function between this measurement and the NLR measurements are plotted. The NLR errors are twice those reported in Table 1 to be conservative. The DMRs of image C and D are consistent with zero, but image B has a low DMR meaning that the radio/mid-IR is anomalously bright with respect to the NLR in this image.

6. Interpretation

There are three possible factors contributing to the anomalous differential magnification ratios we observe. Microlensing of the BLR by stars in the lens galaxy could be changing its magnification ratios relative to those of the NLR, radio and mid-IR. This is discussed in Section 6.1. The size of the NLR could be big enough with respect to the host lens that its magnification differs from that of the other emission regions even without what would normally be classified as substructure. This is ruled out in Section 6.2. Finally, larger scale substructure (possibly made of CDM) either in the lens galaxy or along the line of sight is causing the mismatch between the NLR and radio/mid-IR magnification ratios. This is termed millilensing and is investigated in Section 6.3.

An additional consideration that can be immediately ruled out is that the time delay between images is longer than the typical timescale for variations in the source. Any reasonable lens model for Q2237+0305 gives time delays that are very short, typically less than a day. Recently, a tentative measurement of the time delay has been made using X-ray observations yielding $2.7^{+0.5}_{-0.9}$ hours between image A and B (Dai et al. 2003). This is well below the timescale on which the QSO is expected to vary in any of the wave-bands discussed in this paper.

6.1. Microlensing

Q2237+0305 is exceptional among QSO lens systems in that its lens galaxy is very close to us ($z=0.03$). This makes the BLR particular susceptible to microlensing for two reasons. First, the Einstein radius of the host galaxy in physical units is roughly $\propto D_{ls}D_l/D_s$ which reaches its maximum close to half way to the source. For this reason the images form closer to the center of the galaxy in Q2237+0305 where the star density is particularly high. In addition, the size of a star’s Einstein radius relative to the size of the source goes as $\sqrt{D_{ls}D_s/D_l}$ and so is exceptionally large for Q2237+0305. There is ample evidence that the QSO’s optical continuum is being microlensing in image B of Q2237+0305 (Irwin et al. 1989; Ostensen et al. 1996; Corrigan et al. 1991; Woźniak et al. 2000; Wyithe et al. 2000b). Monitoring has shown that in the optical, image B went from being the second brightest image (hence the name) to being tied for the dimmest image over a two year period. We find image B to be dimmest in the NLR and the BLR. This gives some hint that the BLR magnification is correlated with the microlensing of the optical continuum.

Further evidence of microlensing of the BLR is in Figure 4 where our data is compared to other data. The mid-infrared emission region is believed to be not much larger than the BLR. The lack of strong anomalies in the mid-IR/radio DMRs suggests that the substructure is very small. In addition, the large anomaly in the BLR/NLR image A DMR implies compact and numerous substructures are responsible. Microlensing by stars seems like the most straightforward explanation.

The microlensing interpretation is also consistent with theoretical expectations for this system. An upper limit on the standard deviation of the magnification ratio caused by microlensing for a finite sized source is $\delta m \lesssim 3 \frac{\sqrt{\kappa_*}}{|1-\kappa+\kappa_*|} \frac{\theta_E(M_*)}{\theta_s}$ (Refsdal & Stabell 1997, 1991) where $\theta_E(M_*)$ is the Einstein radius for a star of mass $M_* = \langle M^2 \rangle / \langle M \rangle$, the averaging is done over the distribution of star masses, and κ_* is the dimensionless surface density in stars. The surface density in smoothly distributed dark matter is $\kappa - \kappa_*$. In this case $\theta_E(M_*) = 0.089 \text{ pc}/D_s \sqrt{M_*/M_\odot} = 3.63 \times 10^{-6} \sqrt{M_*/M_\odot} \text{ arcsec}$. Trott & Webster (2002) have modeled the mass distribution of Q 2237+0305 using the QSO image positions and a variety of direct observations of the lens galaxy. Their best fit model gives $\kappa - \kappa_* \simeq 0.05$ and $\kappa_* \simeq 0.04$ at the radius of the images. For a realistic value of $M_* = 0.5 M_\odot$ this gives $\delta m \lesssim 0.04 \text{ pc}/R_{\text{NLR}}$ where R_{NLR} is the physical size of the BLR.

The size of the BLR in some QSOs and Seyfert galaxies can be estimated using reverberation mapping. Combining the radius–luminosity relation and broad line width–luminosity relation of Kaspi et al. (2000) gives $R_{\text{NLR}} \simeq 0.03(4108 \text{ km s}^{-1}/v_{\text{FWHM}})^{2.58} \text{ pc}$ although there is significant scatter about this relation. With the $H\beta$ line widths reported in §4 this gives $R_{\text{NLR}} \sim 0.05 \text{ pc}$, small enough that the the observed magnification of image A can be explained by microlensing.

The time scale for changes in the microlensing magnification is set by the size of the BLR and the velocity of the stars in the galaxy relative to the image. The BLR is of order a light–month in size and typical speeds for the galaxy and rotation of the its disk are $\sim 200 \text{ km s}^{-1}$. This gives a time scale of $\sim 100 \text{ yr}$. This is in contrast to microlensing of the visible continuum where the time scale is about 100 times smaller (Wyithe et al. 2000b, 2000a).

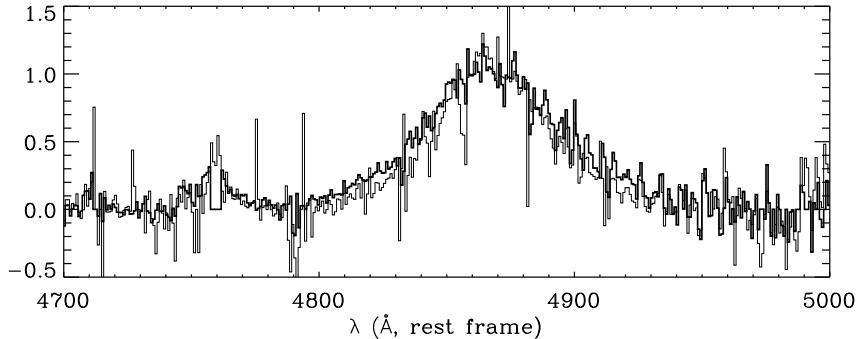


Fig. 6.— Comparison of the $H\beta$ line in image A (dark curve) to that in image B (light curve). The line in image A is slightly wider than the line in image B. This could be caused by a blending of the emission from the NLR and the BLR combined with differing magnifications or by microlensing of kinetically distinct regions of the BLR.

6.1.1. $H\beta$ Line Profiles

Several groups have investigated the possibility of detecting microlensing and learning something about the structure of the BLR through distortions in the profile of the broad lines (Nemiroff 1988; Schneider & Wambsganss 1990; Abajas et al. 2002). If the BLR has a coherent, large scale velocity structure (such as rotation or uniform infall) microlensing could change the shape of a broad line in the image that is being microlensed. This effect comes about because the magnification can vary across the image of the source and the emission region for a narrow range of wavelength can be much smaller than the whole NLR. It was generally thought that if microlensing would have an insignificant effect on the total magnification of the BLR of a bright QSO.

We find that the $H\beta$ line is wider in image A with respect to the other images. Figure 6 shows the line in image A and B with the continuum subtracted and normalized so they have the same height. The change is not large and there is no significant evidence that the asymmetry of the lines are different in the different images. In appendix A an upper limit to the contribution a wavelength dependent component to the magnification is derived. More than half of the anomalous magnification in image A must be caused by a magnification that is uniform over the velocity structure of the $H\beta$ emission region.

The extra width of the image A $H\beta$ line can be interpreted as either caused by the microlensing of a small scale velocity structure in the BLR or as a sign that there is a narrow-line component to the $H\beta$ that is not being magnified as strongly in image A as the broad-line component. The microlensing explanation would not in general produce a symmetric broadening like the one we see, but it is possible that it would. We conclude that there is no strong evidence for coherent large scale motion in the $H\beta$ BLR, but that this possibility cannot be ruled out.

Filippenko (1989) found that the broad $MgII \lambda 2798$ line had a slightly asymmetric distortion in its profile between the different QSO images of Q2237+0305 which could be attributed to microlensing. It is known that the BLR for high ionization states is significantly smaller than

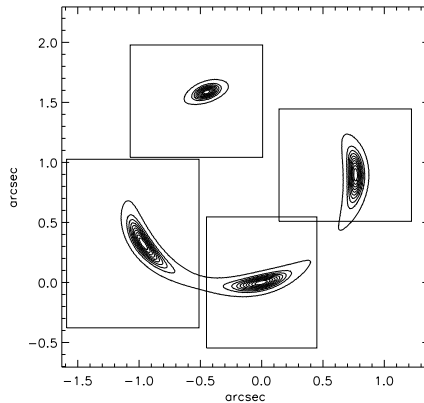


Fig. 7.— A model of Q2237+0305 with the regions used for measuring the magnification ratios shown. In this case the source has a Gaussian profile of size $R_{0.1} = 526$ pc (full width for 10% peak surface brightness). The lowest contour is at 1% of the peak surface brightness and they go up in intervals of 10%. It can be seen that differences in the $\Delta_{NL/BL}$'s from zero are not caused by losses outside of the integration regions.

the $H\beta$ BLR (see Peterson & Wandel 1999, for an illustration of this) thus more susceptible to microlensing and possibly more coherent in its velocity structure.

6.2. NLR size effects

There are two ways in which the size of the NLR might change the NL/BL ratio between images without substructure. First, if the effective size of the NLR is close to the size of the aperture used to measure the flux the NLR/BLR ratio will be affected. Because the sizes of the NLR are different in each image it is possible some of the flux could leak out of the aperture causing the more magnified images to have lower NLR to BLR ratios. This possibility can be eliminated by increasing the size of the apertures and seeing in the NLR fluxes go down as is the case for our extended apertures.

The second possibility is that the NLR is large enough that the magnification cannot be considered uniform over the whole image and thus its total magnification will differ from that of the smaller BLR. To address this issue we model the lens and the NLR for Q2237+0305 and measure the ratios in mock data. The lens model consists of a elliptical halo with a power-law radial profile, a exponential disk and an external shear. The model reproduces the image positions and the radio magnification ratios. The same apertures are used in the simulations and with the data. Figure 7 shows an example of one such simulation. We use two models for the surface brightness profile of the NLR – an exponential and a Gaussian. The Gaussian is meant to represent the case of a NLR with a sharp edge while the exponential is more diffuse. The profile of the NLR of NGC 4151, probably the best studied example in a Seyfert galaxy, is roughly exponential although it does show significant irregularities and asymmetries (Robinson et al. 1994).

The size of the NLR in $C\text{ III] } \lambda 1909$ was inferred from modeling the arc connecting images A, B and D by Mediavilla et al. (1998). They estimate the size of the BLR in this wavelength to be $340 - 570h^{-1}$ pc where this is the total extent of the observed emission. Direct HST measurements of QSOs in $[O\text{ III}]$ indicate that the the NLR could be a few kpc in total extent

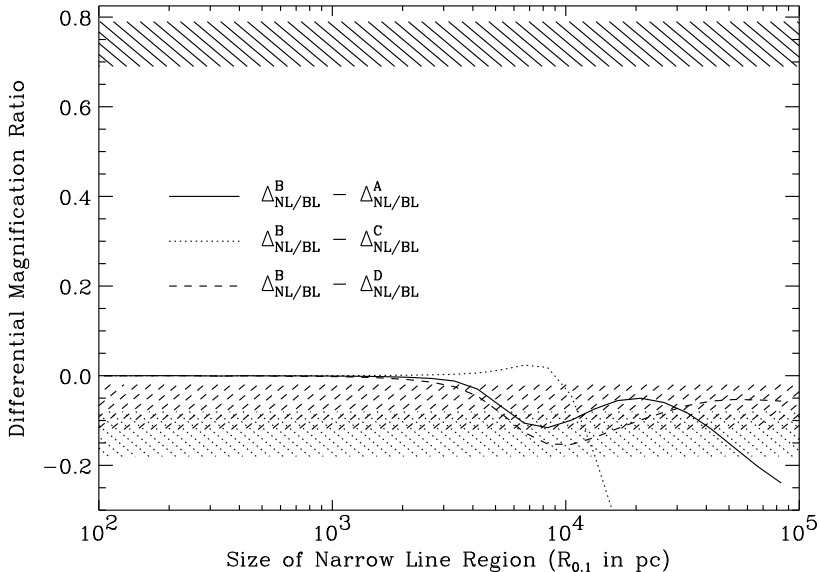


Fig. 8.— The DMRs with respect to image B are plotted as a function of source size, $R_{0.1}$. These are calculated using the lens model and the extended apertures discussed in the text. The source profile is Gaussian in this example. The hashed regions are within 1σ of the measured values.

(Bennert et al. 2002).

Figure 8 shows the results of these simulations along with the observed DMRs. The size of the source is measured by $R_{0.1}$ which is the radius at which the surface density drops below 10%. For comparison $1'' = 24.5h_{65}^{-1}$ kpc on the source plane and $885h_{65}^{-1}$ pc on the lens plane. For a Gaussian source profile the DMR does not differ greatly from one (or zero in magnitudes) if $R_{0.1} \lesssim 4$ kpc. For an exponential profile the same is true for $R_{0.1} \lesssim 2$ kpc. And when the NLR is large enough to change the DMR it is in the opposite direction to the observed A to B DMR. We conclude that the finite size of the NLR could account for the low (but not very low) C to B and D to B DMRs, but not for the high A to B DMR.

6.3. Millilensing

The disagreement between the NLR and radio/mid-IR magnification ratios is most easily explained by the presence of substructure with a mass $m \gg M_{\odot}$. We shall see that the quantity of substructure required to make this discrepancy probable makes substructure made of CDM a more likely explanation than substructure composed of ordinary gas and stars such as dwarf galaxies or globular clusters. To determine the level and properties of the substructure that are compatible with the measured DMRs we carry out extensive lensing simulations.

6.3.1. simulations

For the results that follow, the magnification distributions were calculated using an adaptive grid code. The strategy is to first calculate the image positions, through the lens equation,

on a coarse grid over the image plane. The deflection angle is found by summing over all the subclumps in this initial region. The grid is then refined to cover smaller regions surrounding each of the images. The grid is made finer when the image begins to cover a large fraction of the gridded region. This process is repeated until enough grid points are within the image to calculate its area to better than 1% accuracy. The magnification is then the ratio between this area and the original area of the unlensed source.

If the substructure is massive ($\gtrsim 10^7 M_\odot$) it can change the position of the images enough that the contribution of the host lens to the image magnification can change. In addition, a single one of these large substructures can affect the magnification of more than one image. For these reasons we simulate the whole lens (host lens plus substructure) at once. In this way we can measure the positions of the images which become significant constraints on the substructure when its mass is large.

CDM simulations predict that most of the substructure at a projected galactic radius of a few kpc will be at a three dimensional radius of a few tens of kpc (Zentner & Bullock 2003). The substructure will then be distributed fairly uniformly on the scale of the host’s Einstein radius. For this reason we do simulations with a constant number density of substructures. We do not characterize the simulations by the mass fraction in substructure because this can vary by a factor of several between the different images owing to the differences in density at small radii. The substructures are modeled as singular isothermal spheres (SISs) tidally truncated as if they are at a distance of 30 kpc from the center of an isothermal galaxy. The lensing is not critically dependent on the details of this truncation. All the substructures are of the same mass. In a more theoretically motivated model there would be a distribution of substructure masses, but in this paper we are seeking to put empirical constraints on the substructure mass scale.

6.3.2. radial profile degeneracy

There is a degeneracy between the level of substructure and the radial profile of the host lens as discussed in Metcalf (2003). The effect of changing the radial profile is investigated by adjusting the host lens model. We start with an elliptical lens model with an $\kappa(\rho) \propto \rho^{-1}$ (where ρ in coordinates that are aligned with the axis of the lens is $\rho^2 = x_1^2 + x_2^2/(1 - \epsilon)^2$) profile that fits the image positions very well. This is known as a singular isothermal ellipsoid (SIE) lens model. We then add a uniform surface density, σ , to the lens and adjust the normalization of the ellipsoidal component so that the image positions do not change. This is always possible and has no effect on the magnification ratios, but it does change the total magnification such that flatter profiles have higher magnifications and it changes the time delays such that flatter profiles have shorter time delays. The total magnification is unobservable and the time delay has not been measured for Q2237+0305. These degenerate models are labeled by their effective logarithmic slope, n_{eff} , which is related to the the added surface density by $n_{\text{eff}} = (\sigma - 1)$. For further discussion see Metcalf (2003).

For each choice of substructure properties and host lens model we run simulations with three different source sizes – 10 pc which is appropriate for the radio and mid-IR emission regions and for the NLR we use 200 pc and 400 pc for all. This size should be viewed as an effective size for the purposes of lensing not the full extent of the NLR which must be larger.

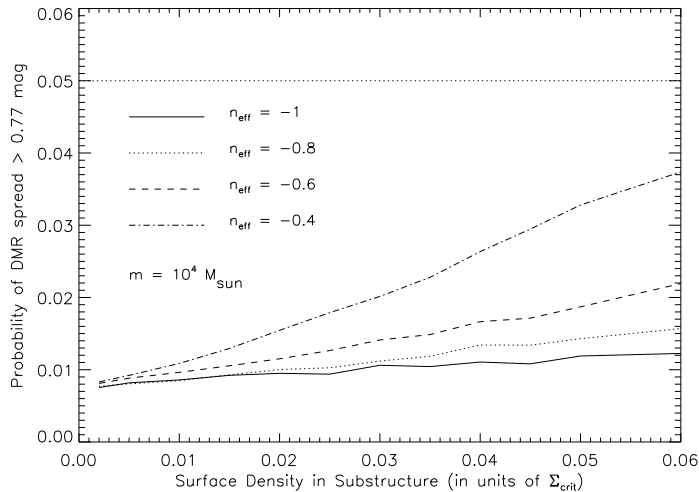


Fig. 9.— The probability that the spread in the DMRs, \mathcal{S} , will be greater than the observed 0.77 mag, $P(\mathcal{S} \geq 0.77 | \kappa_{\text{sub}}, n_{\text{eff}}, m)$, with substructure mass $m = 10^4 M_{\odot}$. The different curves are for host lens models with different radial profiles (see Section 6.3.2). The horizontal dotted line marks the 5% level for reference. To convert the surface densities into mass fractions in substructure see Table 3.

Image	$n_{\text{eff}} =$	-1.0	-0.8	-0.6	-0.4	-0.2
A	$\kappa =$	0.4	0.5	0.6	0.8	0.9
B	$\kappa =$	0.4	0.5	0.6	0.8	0.9
C	$\kappa =$	0.7	0.8	0.8	0.9	0.9
D	$\kappa =$	0.6	0.7	0.8	0.8	0.9

Table 3: The surface densities at each of the images in units of $\Sigma_{\text{crit}} (= 9.8 \times 10^3 M_{\odot} \text{ pc}^{-2}$ in the $H_o = 70 \text{ km s}^{-1} \text{ Mpc}^{-1}$, $\Omega_{\Lambda} = 0.7$, $\Omega_{\text{matter}} = 0.3$ cosmology. These values differ from those in the lens model of Schmidt, Webster, & Lewis (1998) at the 10% level. The $n_{\text{eff}} = -1$ model is the singular isothermal ellipsoid lens model.

6.3.3. results

We find that the data are best suited to putting a lower limit on the surface density of substructure as a function of the substructure mass and the host lens profile; this is the most robust and conservative way to treat the data. To quantify this we use the *spread* statistic. We define the spread, \mathcal{S} , as the difference between the largest DMR and the smallest, including the normalization image’s DMR ($\Delta = 0$). This statistic is clearly independent of which image is used to normalize the DMRs. In the absence of substructure and noise $\mathcal{S} = 0$. As shown in Section 5 the measured spread is $\mathcal{S} = 0.77$ mag. We calculate the probability of getting an observed spread as large as this or larger given the level of substructure and the noise, $P(\mathcal{S} \geq 0.77)$. This is done by Monte Carlo, using the simulations to predict the flux of each image and then adding random noise. At least 2,000 lensing simulations are calculated for each choice of substructure parameters and for each simulation 500 realizations of the noise are made. The results do not change when these numbers are increased. To be conservative we use twice the NLR flux errors derived from the data and reported in Table 1.

Figures 9 through 13 show the probability $P(\mathcal{S} \geq 0.77)$ for different substructure masses.

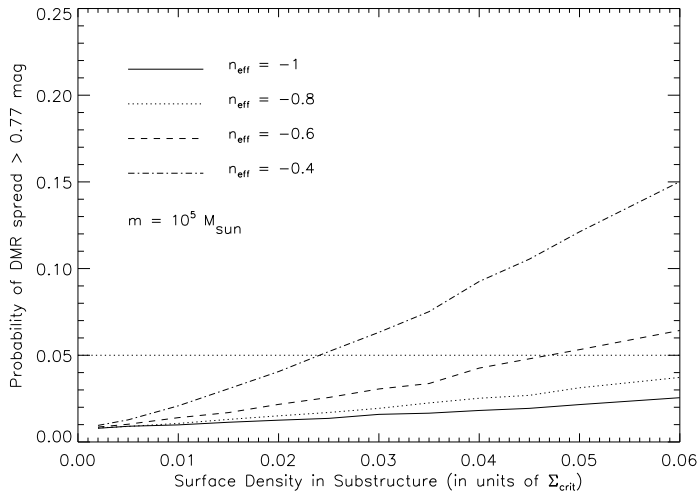


Fig. 10.— Same as in Figure 9 only with substructure mass $m = 10^5 M_\odot$. Note that the scale is different and the probabilities are generally larger.

ℓ_{NLR} (pc)	200	200	200	200	400	400	400	400
n_{eff}	-1.0	-0.8	-0.6	-0.4	-1.0	-0.8	-0.6	-0.4
$10^4 M_\odot$	> 0.06	> 0.06	> 0.06	> 0.06	> 0.06	> 0.06	> 0.06	> 0.06
$10^5 M_\odot$	> 0.06	> 0.06	0.047	0.024	> 0.06	> 0.06	0.047	0.024
$10^6 M_\odot$	0.029	0.020	0.013	0.007	0.034	0.023	0.015	0.008
$10^7 M_\odot$	> 0.06	0.037	0.024	0.011	0.053	0.030	0.017	0.007
$10^8 M_\odot$	–	–	0.034		–	0.035	0.019	

Table 4: Minimum substructure surface densities required to have a better than 5% chance of observing a DMR spread as large as the one observed. The cases marked “> 0.06” did not reach this limit within the range of surface densities tested, those marked “–” appear as though they cannot reach this limit for any κ_{sub} and those that are blank where not tested because the images tended to merge in too many cases.

Figure 9 is for a mass of $10^4 M_\odot$. In this case the substructures are not large enough to change the magnification of the NLR and only rarely can significantly change the magnification of the 10 pc source representing the radio and mid-IR sources. The probability is correspondingly low with none of the models going above 5% probability for $\kappa_{\text{sub}} < 0.06$. We consider this low probability unacceptable thus ruling out $m = 10^4 M_\odot$ substructure with $\kappa_{\text{sub}} < 0.06$ as an explanation. To translate these values into mass fractions Table 3 gives the surface densities at each image in the different models.

Figure 10 shows the probabilities for mass $10^5 M_\odot$. The probability is larger here than for $10^4 M_\odot$, but still not significant unless the host halo is flatter than an SIE. The $n_{\text{eff}} = -1$ model, the most common assumption in lensing, is ruled out for the range of κ_{sub} tested. Our maximum surface density of $\kappa_{\text{sub}} = 0.06$ is still very large compared to the some CDM predictions of less than 0.1% at this mass scale (Zentner & Bullock 2003). The $n_{\text{eff}} = -0.4$ case reaches our threshold of 5% at $\kappa_{\text{sub}} = 0.047$ making this the lower limit in this case.

A mass of $10^6 M_\odot$ is investigated in Figure 11. In this case for substructure surface densities

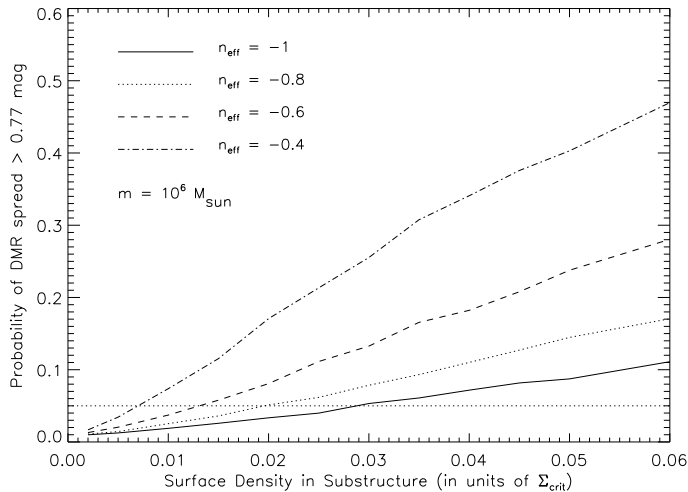


Fig. 11.— Same as in Figure 10 only with substructure mass $m = 10^6 M_{\odot}$.

$\kappa_{\text{sub}} > 0.029$ the observed DMR discrepancy occurs more than 5% of the time in all the host models tested. At the 10% level $\kappa_{\text{sub}} > 0.058$ in the most common $n_{\text{eff}} = -1$ model. For flatter models this lower limit is reduced significantly. These are more reasonable mass fractions since $\kappa_{\text{sub}} = 0.02$ corresponds to $f_{\text{sub}} \simeq 0.05$ at image A in the $n_{\text{eff}} = -1$ model and less in the flatter models. However, at this mass scale this is still rather large compared to the current CDM predictions.

Figure 12 shows $P(S \geq 0.77)$ for substructure of mass $10^7 M_{\odot}$. In this case the substructure is big enough to occasionally shift the image positions by a few tenths of an arcsec. Lens models for Q2237+0305 using the observed distribution of stars have been very successful at reproducing the image positions (Trott & Webster 2002; Schmidt et al. 1998). For this reason any substructure cannot change the image position by very much. In Figure 12 limits on the allowed shift in image positions are imposed to express this additional constraint. We adopt a conservative limit of $0''.2$ as a test. Results with and without the image shift constraint are plotted in Figure 12 and it is seen that this extra constraint does not change the lower limits on κ_{sub} . The most striking result displayed in Figure 12 is that the $n_{\text{eff}} = -1$ is unlikely to produce the observations for any substructure surface density that is reasonable from the prospective of current CDM model predictions ($\kappa_{\text{sub}} = 0.06$ would be 15% of the mass at image A). In fact, $P(S \geq 0.77)$ does not go above 15% within the range of κ_{sub} investigated unless $n_{\text{eff}} \geq -0.4$. In some cases we can put an upper limit on κ_{sub} and they are reported in Table 4.

Figure 13 shows $P(S \geq 0.77)$ substructure of mass $10^8 M_{\odot}$. Here all the models are ruled out at the 90% level and the only way to get above the 95% level is to abandon a limitation on the shift of the image position which we think is not realistic. High mass substructure is not compatible with the observed DMRs because it is not effective in changing the small and large scale magnification ratios independently - when it magnifies (or demagnifies) the radio and mid-IR images it also magnifies (or demagnifies) the NLR image. This is further conformation that anomalous DMRs must be the results of small scale structure and not a large scale distortion of the host lens. In addition, the $10^8 M_{\odot}$ substructure tends to displace the images on the scale of several tenths of an arcsec although this mass range is ruled out even

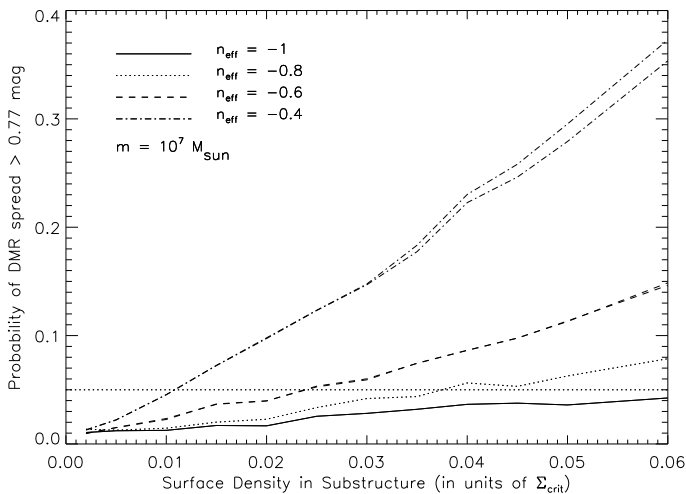


Fig. 12.— Same as in Figure 11 only the substructure mass is $10^7 M_{\odot}$ and two limits on the shift of the image positions are shown. For each n_{eff} the lowest curve is for a $0''.2$ limit and the highest is for no limit. For the $n_{\text{eff}} = -1, -0.8$ and -0.6 the $0''.2$ limit is indistinguishable from no limit. Note that scale in this plot is not the same as in Figure 11.

without this constraint.

We have done these calculations with source sizes of 200 pc and 400 pc representing the NLR. Changing the size makes only small changes to $P(\mathcal{S} \geq 0.77)$ at large mass and large n_{eff} . These changes do not significantly change the conclusions. For Figures 9 through 13 the NLR source size is set to 200 pc. The lower limits on κ_{sub} for all the models tested are shown in table 4.

The error estimates that have been derived for our observations and those published with the mid-IR and radio observations are crucial for the estimation of the surface density bound. If the errors are underestimated the κ_{sub} lower bound should be lower. For example, if we increase the radio errors of Falco et al. (1996) by half the κ_{sub} lower limit in the $n_{\text{eff}} = -1, m = 10^6 M_{\odot}$ model goes from 0.029 to 0.021. Increasing the mid-IR errors (Agol et al. 2000) in this way changes this limit to 0.016. On the other hand if the empirically derived errors on our NLR measurements are used instead of doubling them the limit is increased to 0.055.

To squeeze more out of the data we can also calculate likelihood functions for the substructure parameters although this is somewhat less robust than the $P(\mathcal{S} \geq 0.77)$ analysis done above. The likelihood function for set of parameters $\{\kappa_{\text{sub}}, n_{\text{eff}}, m\}$ is given by

$$\mathcal{L}(\kappa_{\text{sub}}, n_{\text{eff}}, m) = \int d\{\text{DMR}\} P_{\text{sub}}(\{\text{DMR}\}, \{\mathbf{x}\} | \kappa_{\text{sub}}, n_{\text{eff}}, m) \times P_{\text{ob}}(\{\text{DMR}_{\text{ob}}\}, \{\mathbf{x}_{\text{ob}}\} | \{\text{DMR}\}, \{\mathbf{x}\}) \quad (2)$$

where P_{ob} expresses the instrumental uncertainties which is taken to be a normal distribution. Uniform prior distributions have been assumed for the parameters. Again the integral is done by Monte Carlo.

Figure 14 shows the likelihoods as functions of substructure mass in several ranges of substructure surface density. Plotted this way it is clear that the data favors a substructure mass of $\sim 10^6 M_{\odot}$ for fixed κ_{sub} . Here the errors in the NLR magnification ratios have been

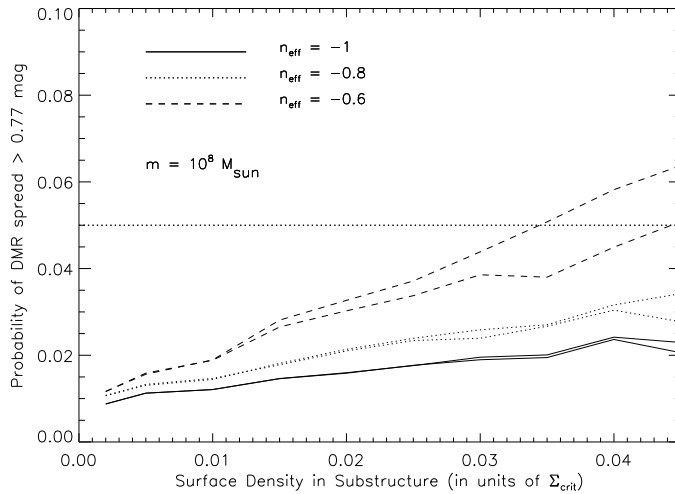


Fig. 13.— Same as in Figure 12 except the substructure mass is $10^8 M_\odot$. None of the models reached above 0.065 probability that the DMRs spread will be greater than 0.77 mag.

set to twice those in Table 1 to be conservative. The likelihood functions with the measured statistical errors are shown in Figure 15. The shape of the likelihood function is very similar, but the extreme masses are more strongly ruled out.

In summary, the data puts a lower limit on the amount of substructure that is present in Q2237+0305. Table 4 gives these limits for the ranges of parameters tested. Given the present CDM simulations these limits seems uncomfortably large. With the expected substructure level of $< 1\%$ of the surface density in subclumps of mass less than $10^8 M_\odot$ the host lens profile as steep as $\kappa(\rho) \propto \rho^{-1}$ is unacceptable. We also find that a substructure mass scale of $\sim 10^6 M_\odot$ is most effective at changing the observed DMRs. Substructure of mass $10^4 M_\odot$ is too small and $10^8 M_\odot$ is too large. The details of the lower mass limit is dependent on our assumption that the radio and mid-IR emission regions are 10 pc in radius, however to the precision we are now concerned with this should not be a major factor.

It has been assumed here that the substructure is within or near the lens galaxy. It is possible that the responsible objects are in intergalactic space either in front of or behind the lens. Within the CDM model this is less probable, but not improbable. The above constraints can be crudely converted to a redshift z by scaling the substructure mass and surface density by a factor of $\Sigma_{\text{crit}}(z_s, z_l)/\Sigma_{\text{crit}}(z_s, z) = \frac{D(z)\{D_s - D(z)\}}{D_l\{D_s - D_l\}}$. This factor reaches a minimum of 0.6 at $z = 1.1$.

6.3.4. The contribution of known objects

There are known objects in our galaxies and others which could conceivably be causing the observed anomalies in the DMRs. One possibility is globular clusters. However, the total mass in globular clusters around the Milky Way is only $\sim 10^7 - 10^8 M_\odot$ so their surface density is two order of magnitude below the lower limits reported here.

Another contribution is from Giant Molecular Clouds (GMCs) of mass $\sim 10^6 M_\odot$ which are known to contain most of the H_2 gas mass in the Milky Way. The surface density of H_2

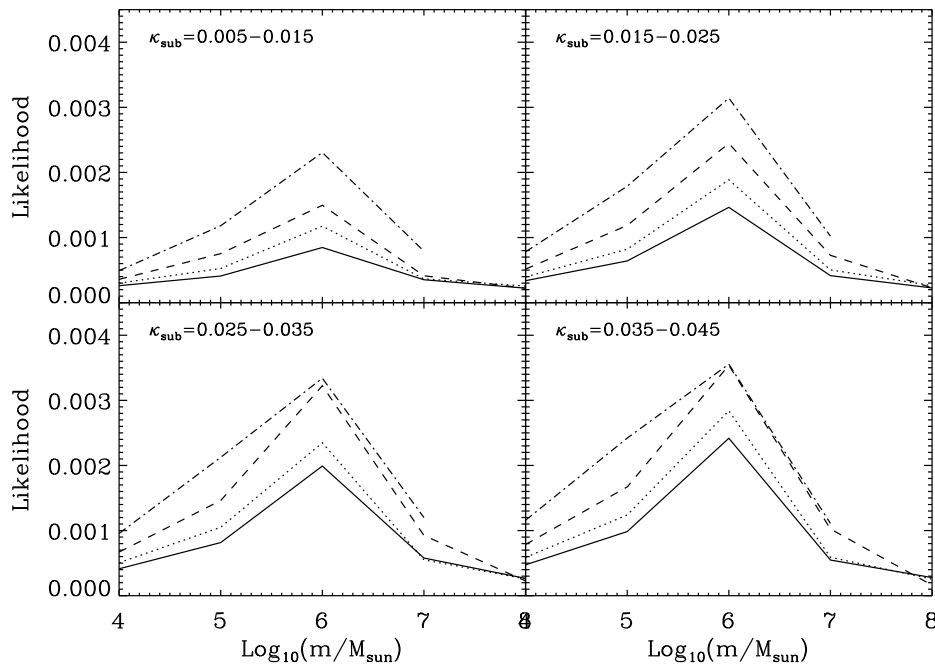


Fig. 14.— These are the likelihood functions for four ranges of substructure surface density as marked in each panel. The curves are marked in the same way as in Figures 9 through 13 – solid: $n_{\text{eff}} = -1$, dotted: $n_{\text{eff}} = -0.8$, dashed: $n_{\text{eff}} = -0.6$ and dot-dashed: $n_{\text{eff}} = -0.4$. The limit in the acceptable shift in the image positions is $0''.2$. The normalization is arbitrary, but all the models are normalized in the same way so that they can be compared between panels. A substructure mass of $\sim 10^6 M_{\odot}$ is clearly favored in all cases.

at galactic radius $\simeq 1$ kpc (where the images in Q2237+0503 form) is only a few $M_{\odot} \text{ pc}^{-2}$, well below our lower limits (Blitz 1997). The H_2 density in M31 no more than $\simeq 5 M_{\odot} \text{ pc}^{-2}$ anywhere (Loiarnard et al. 1999). However, in some galaxies the peak H_2 density does exceed our lower limit (Helfer et al. 2003). The H_2 density is truncated at an inner radius of several kpc. This is believed to be caused by the galactic bar. The same phenomena is seen in other barred spirals. In Q2237+0503 the lensing is almost entirely caused by the bulge and bar of the galaxy through which the images pass (Trott & Webster 2002). For this reason we expect the density of GMCs to be well below our limit. In addition, GMCs are not very centrally concentrated, they are generally held up by turbulent pressure and have many, much smaller mass, condensations sprinkled throughout them. For this reason GMCs make inefficient lenses as compared to the SIS model used in Section 6.3.1 through 6.3.3. The GMCs would need more density by a factor of a few to reproduce reproduce the lensing observations.

Another argument for a small surface density in GMCs is the extinction. By adopting an upper limit on the absolute luminosity of the QSO of $M_B > -29$ and an upper limit of 20 for the lens magnification (the SIE+shear model predicts 16) an upper limit for the extinction of $A_V < 2.7$ mag can be derived (Falco et al. 1999). The extinction in the Milky Way is roughly related to the hydrogen column density through $N(\text{HI}) + 2N(\text{H}_2) \simeq 13 A_V M_{\odot} \text{ pc}^{-2}$ (Savage et al. 1977). Conservatively assuming all the hydrogen is in molecular form this gives an upper limit of $N(\text{H}_2) < 18 M_{\odot} \text{ pc}^{-2}$ which is well below our lower limit on substructure. Falco et al. (1999) have argued that the above relation between hydrogen column density and extinction

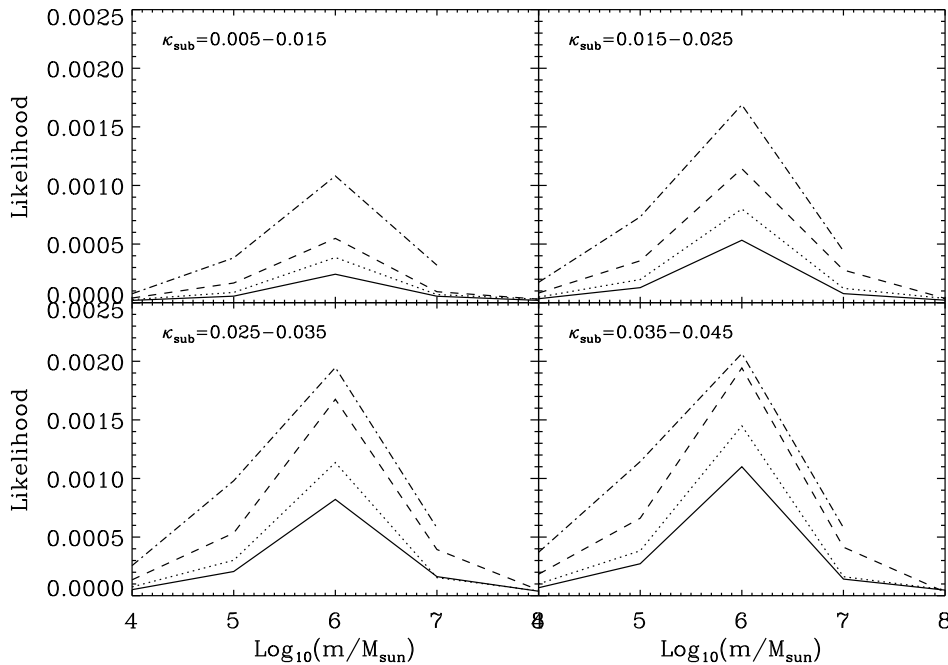


Fig. 15.— The same as in Figure 14 only the errors for the NLR magnification ratios reported in Table 1 are used instead of doubling them to account for unknown systematic errors. The normalization is arbitrary and different from that in Figure 14.

does not hold for some of the lens galaxies they studied in the sense that it over estimates the column density which makes our upper limit even more conservative.

For the above reasons we do not think GMCs are a likely explanation for the DMR anomalies, but they are probably the largest potential “background” and we plan to investigate their lensing properties more thoroughly in the future. For lenses with elliptical galaxies – the majority of QSO lenses – GMCs are much less likely to be a source of lensing substructure. Analyzing more lens systems can definitively rule of GMCs.

7. Discussion

We have demonstrated the spectroscopic gravitational lensing method and shown the importance of having high quality data in a large range of wavelength. Using the CIRPASS instrument the magnification ratios of the QSO’s narrow lines region and broad line region were measured. It was found that these do not agree with each other or with the published radio and mid-IR magnification ratios. The disagreement between the BLR magnification ratios and the radio/mid-IR magnification ratios is interpreted as microlensing of the BLR. This implies that the mid-IR emission region is larger than the BLR and the BLR is $\lesssim 0.1$ pc in size. We find a small difference in the shape of the $H\beta$ line in image A when compared to the other images. This difference is too small and symmetric to be considered evidence for rotation or large scale infall in the $H\beta$ emission region. The disagreement between the radio/mid-IR ratios and the NLR ratios is interpreted as a signature of substructure. Lensing simulations are performed to obtain a lower limit on the amount and mass of substructure that is required to cause this discrepancy. The substructure content is degenerate with the radial profile of the host lens, but if the

expectations of the CDM model are taken into account certain radial profiles and substructure surface densities can be ruled out. The substructure mass scale as large as $10^8 M_\odot$ and $10^7 M_\odot$ is disfavored while $10^4 M_\odot$ is too small given our assumptions about the radio/mid-IR source size. The standard elliptical singular isothermal lens mass profile is disfavored in comparison to a more flattened profile with the same substructure content.

Although the anomalous differential magnification ratios in Q2237+0305 are very unlikely to be caused by a substructure as large as $10^8 M_\odot$ this does not mean that the mass function of substructures does not extend up to this mass scale. Large mass substructures could dominate the total mass in substructure and yet be very few in number so that one would expect many lenses to be unaffected by them; in other words the shot noise from lens to lens is expected to be large at high masses. If the responsible object is intergalactic and unassociated with the lens galaxy the mass bound is different, but in this case the upper mass bound is more likely to go down then up because the lens galaxy is unusually close to us and not near the minimum of $\Sigma_{\text{crit}}(z_s, z)$.

It should be mentioned that flattening the host lens' radial mass distribution generally reduces the Hubble parameter as measured by the time delays. The X-ray measurement of the time delay ($2.7_{-0.9}^{+0.5}$ hours between image A and B) is tentative (Dai et al. 2003), but it does indicate that Q2237+0305 has a near r^{-1} surface density profile if the HST Key Project's value for the Hubble parameter is used ($72 \pm 8 \text{ km s}^{-1} \text{ Mpc}^{-1}$; Freedman et al. 2001). The fiducial SIE+shear model used here gives a time delay of 3.3 hours and the delay is proportional to n_{eff}^{-1} as defined in section 6.3.2. In general the measured time delays in other lenses lead to a conclusion that either the Hubble parameter is smaller than the above value or the profile is steeper than r^{-1} . Kochanek (2003) has highlighted this as a problem for the CDM model. This is an unresolved and intriguing problem which becomes even more so with our results since the steeper the radial profile the more substructure is needed. It could be that in looking for substructure to confirm CDM we have found too much.

Clearly more lens systems need to be studied in this way to put stronger constraints on dark matter substructure and eliminate systematics. The prospects for improvement are good in this respect since Q2237+0305 is not an ideal system for this work – the [O III] lines are in a region of high atmospheric absorption and because of the proximity of the lens galaxy microlensing is enhanced. The situation can be greatly improved with just a few more systems observed in narrow lines and the mid-IR and/or radio. One of the most important systematic uncertainties we encountered is how to construct the apertures around each of the images for measuring the magnification ratios. The improved spatial resolution that would come with using a space-based observations (or with adaptive optics-enhanced spectroscopy from the ground) would be of great benefit in reducing this uncertainty.

A. Contribution of Wavelength Dependent Magnification

It is possible that the magnification of the BLR is not uniform as would probably be the case if microlensing is important and the BLR size is of order the Einstein radius of the stars in the lens galaxy. This possibility can be tested if the BLR has a coherent large scale velocity structure as in the case of a rotating disk or spherical infall. In this case a small scale variation in the magnification would distort the the broad line in one or more of the images. This effect was proposed by Nemiroff (1988). The contribution of such a wavelength dependent magnification to the differential magnification ratio can be assessed by comparing the line profiles from the

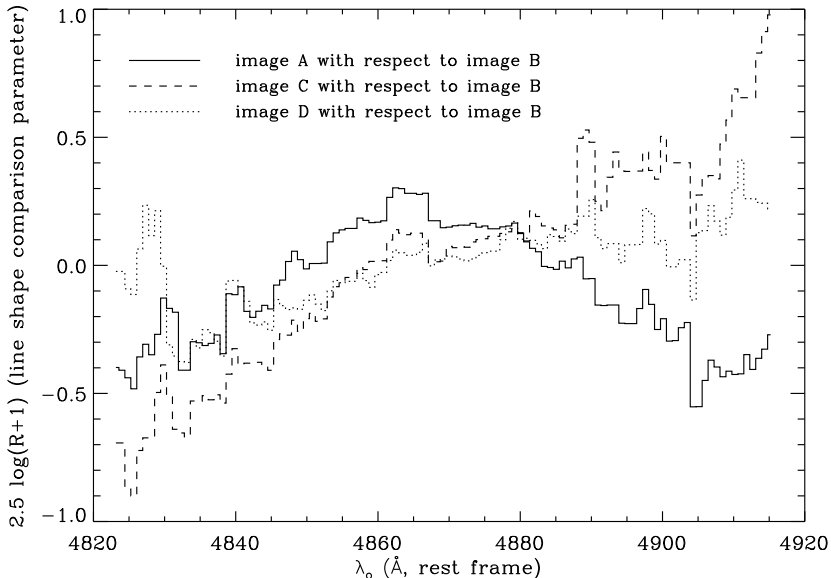


Fig. 16.— The line profile distortion parameter, equation A1, between image A and the other images. The central peak is 0.3 mag which indicates that the wavelength independent contribution to the NLR/BLR differential magnification ratio is at minimum 0.3 mag.

two images.

If the wavelength of the i th pixel of a spectrum is λ_i then the flux in this pixel is $F(\lambda_i) = \mu(\lambda_i)f(\lambda_i)$ where $f(\lambda_i)$ is the flux before magnification and $\mu(\lambda_i)$ is the magnification at that wavelength. The total flux from the BLR is $F = \sum_i F(\lambda_i)$. We will assume that one of the BLR images is uniformly magnified, i.e. the magnification is not a function of wavelength. To be specific we will label this image B although it could be any image or an average of some of the images. For this image $F^B(\lambda_i)/F^B(\lambda_o) = f(\lambda_i)/f(\lambda_o)$ where λ_o is a reference pixel that can be varied. Because the pre-lensed line profile, $f(\lambda_i)$, is the same for all the images we can calculate the change to the total flux in image A caused by a frequency dependent magnification:

$$R(\lambda_o) \equiv \frac{F^A - F_o^A}{F_o^A} = \frac{F^B(\lambda_o)F^A}{F^A(\lambda_o)F^B} - 1 \quad (\text{A1})$$

where F_o^A is what the total flux would be if the magnification were uniform and equal to $\mu^A(\lambda_o)$. Another way to think of this quantity is to note that if you wanted to correct the observed differential magnification ratio (with the sign convention used in this paper) to what it would be if the BLR magnification ratio were uniformly $\mu^B/\mu^A(\lambda_o)$ then one would subtract $2.5 \log[R(\lambda_o) + 1]$ magnitudes. After subtracting the continuum and masking any sky lines equation (A1) can be applied directly to the data to determine if a wavelength dependent component of the magnification is causing a significant change in the line flux. Figure 16 shows this for our data.

Microlensing is not the only thing that could affect the line profiles. Within the broad line there is also a contribution from the NLR. This NLR contamination will reduce the magnitude of the differential magnification ratio, diluting any signal from substructure. It will also make images with relatively bright BLRs have a wider line profiles as is observed in our data

(Figure 6). If we use a simple model where there is a distinct NLR and BLR in $H\beta$ (which is probably not the case) and we denote their magnifications as μ_{NL} and μ_{BL} respectively then the expected shape parameter will be

$$R(\lambda_o) = \frac{(\omega(\lambda_o) - \omega)(r^A - r^B)}{(\omega(\lambda_o) + r^A)(\omega + r^B)} \quad (\text{A2})$$

where $\omega = f_{\text{NL}}/f_{\text{BL}}$ and $r = \mu_{\text{BL}}/\mu_{\text{NL}}$. Note that if the NLR and BLR components of the line are both symmetric then this effect will not make the line asymmetric. More generally, since the NL is narrow by definition the line profile should only be modified in the central region.

It is also interesting to note that in the limit that $\omega \rightarrow 0$ while the central wavelength is still dominated by the NL ($\omega(\lambda_{H\beta}) \rightarrow \infty$) $R(\lambda_{H\beta}) = \text{DMR} - 1$. With our data this would give an estimate of $\text{DMR} = 0.3$ mag between A and B images - still well above the noise. This is a lower limit since as the dominance of the NL at the central wavelength, $\omega(\lambda_{H\beta})$, is reduced the implied DMR becomes larger.

Acknowledgments

This paper is based on observations obtained at the Gemini Observatory, which is operated by the Association of Universities for Research in Astronomy, Inc. (AURA), under a cooperative agreement with the U.S. National Science Foundation (NSF) on behalf of the Gemini partnership: the Particle Physics and Astronomy Research Council (UK), the NSF (USA), the National Research Council (Canada), CONICYT (Chile), the Australian Research Council (Australia), CNPq (Brazil) and CONICET (Argentina). We are grateful to Matt Mountain for the Director’s discretionary time to demonstrate the scientific potential of integral field units (the PIs of this demonstration science program are Andrew Bunker, Gerry Gilmore and Roger Davies). We thank the Gemini Board and the Gemini Science Committee for the opportunity to commission CIRPASS on the Gemini-South telescope as a visitor instrument. We received excellent support from Gemini, and thank Phil Puxley, Jean René-Roy, Doug Simons, Bryan Miller, Tom Hayward, Bernadette Rodgers, Gelys Trancho, Marie-Claire Hainaut-Rouelle and James Turner. CIRPASS was built by the instrumentation group of the Institute of Astronomy (IoA) in Cambridge, UK. We warmly thank the Raymond and Beverly Sackler Foundation and PPARC for funding this project. Andrew Dean, Rob Sharp, Anamparambu Ramaprakash and Anthony Horton all assisted with the observations in Chile, and we are indebted to Dave King, Jim Pritchard & Steve Medlen for contributing their instrument expertise. The optimal extraction software for this 3D fiber spectroscopy was written by Rachel Johnson, Rob Sharp and Andrew Dean. We would like to thank J. Primack for providing access to the UC Santa Cruz beowolf computer cluster. RBM would like to thank the IoA for hosting him during part of the preparation of this paper and P. Natarajan for helpful discussion. LAM acknowledges support from the SIRTf Legacy Science Program provided through an award issued by Jet Propulsion Laboratory, California Institute of Technology, under NASA contract 1407. Financial support for RBM was provided by NASA through Hubble Fellowship grant HF-01154.01-A awarded by the Space Telescope Science Institute, which is operated by the Association of Universities for Research in Astronomy, Inc., for NASA, under contract NAS 5-26555

REFERENCES

- Abajas, C., Mediavilla, E., Muñoz, J. A., Popović, L. Č., & Oscoz, A. 2002, *ApJ*, 576, 640
- Agol, E., Jones, B., & Blaes, O. 2000, *ApJ*, 545, 657
- Andreani, P., Franceschini, A., & Granato, G. 1999, *MNRAS*, 306, 161
- Antonucci, R. 1993, *ARA&A*, 31, 473
- Bennert, N., Falcke, H., Schulz, H., Wilson, A. S., & Wills, B. J. 2002, *ApJ*, 574, L105
- Blitz, L. 1997, in *CO: Twenty-Five Years of Millimeter-Wave Spectroscopy*, ed. W. Latter et al., IAU Symp No. 170 (Kluwer Academic Publishers), 11–18
- Boroson, T. A. & Green, R. F. 1992, *ApJS*, 80, 109

- Bradač, M., Schneider, P., Lombardi, M., Steinmetz, M., Koopmans, L., & Navarro, J. 2003, preprint, astro-ph/0306238
- Bullock, J. S., Kravtsov, A. V., & Weinberg, D. H. 2000, *ApJ*, 539, 517
- Chiba, M. 2002, *ApJ*, 565, 17
- Corrigan, R. T., Irwin, M. J., Arnaud, J., Fahlman, G. G., Fletcher, J. M., Hewett, P. C., Hewitt, J. N., Le Fevre, O., et al. 1991, *AJ*, 102, 34
- Dai, X., Chartas, G., Agol, E., Bautz, M. W., & Garmire, G. P. 2003, *ApJ*, 589, 100
- Dalal, N. & Kochanek, C. S. 2002, *ApJ*, 572, 25
- Dong, S., Murray, S., & Lin, D. 2003, preprint
- Falco, E. E., Impey, C. D., Kochanek, C. S., Lehár, J., McLeod, B. A., Rix, H. ., Keeton, C. R., Muñoz, J. A., et al. 1999, *ApJ*, 523, 617
- Falco, E. E., Lehar, J., Perley, R. A., Wambsganss, J., & Gorenstein, M. V. 1996, *AJ*, 112, 897
- Filippenko, A. V. 1989, *ApJ*, 338, L49
- Freedman, W. L., Madore, B. F., Gibson, B. K., Ferrarese, L., Kelson, D. D., Sakai, S., Mould, J. R., Kennicutt, R. C., et al. 2001, *ApJ*, 553, 47
- Gaudi, B. S. & Petters, A. O. 2002, *ApJ*, 580, 468
- Helfer, T. T., Thornley, M. D., Regan, M. W., Wong, T., Sheth, K., Vogel, S. N., Blitz, L., & Bock, D. C.-J. 2003, *ApJS*, 145, 259
- Huchra, J., Gorenstein, M., Kent, S., Shapiro, I., Smith, G., Horine, E., & Perley, R. 1985, *AJ*, 90, 691
- Irwin, M. J., Webster, R. L., Hewett, P. C., Corrigan, R. T., & Jedrzejewski, R. I. 1989, *AJ*, 98, 1989
- Johnson, R. et al. 2003, in preparation
- Kaspi, S., Maoz, D., Netzer, H., Peterson, B. M., Alexander, T., Barth, A. J., Bertram, R., Cheng, F.-Z., et al. 1996, *ApJ*, 470, 336
- Kaspi, S., Smith, P. S., Netzer, H., Maoz, D., Jannuzi, B. T., & Giveon, U. 2000, *ApJ*, 533, 631
- Klypin, A., Kravtsov, A. V., Bullock, J. S., & Primack, J. R. 2001, *ApJ*, 554, 903
- Kochanek, C., Falco, E., C., I., Lehar, J., McLeod, B., & Rix, H.-W. 2000, CASTLES Survey, <http://cfa-www.harvard.edu/castles/>
- Kochanek, C. S. 2003, *ApJ*, 583, 49
- Loinard, L., Dame, T. M., Heyer, M. H., Lequeux, J., & Thaddeus, P. 1999, *A&A*, 351, 1087
- Mao, S. & Schneider, P. 1998, *MNRAS*, 295, 587
- Maoz, D., Smith, P. S., Jannuzi, B. T., Kaspi, S., & Netzer, H. 1994, *ApJ*, 421, 34
- Mediavilla, E., Arribas, S., del Burgo, C., Oscoz, A., Serra-Ricart, M., Alcalde, D., Falco, E. E., Goicoechea, L. J., et al. 1998, *ApJ*, 503, L27
- Metcalf, R. 2003, in preparation
- Metcalf, R. B. & Madau, P. 2001, *ApJ*, 563, 9
- Metcalf, R. B. & Zhao, H. 2002, *ApJ*, 567, L5
- Moore, B., Quinn, T., Governato, F., Stadel, J., & Lake, G. 1999, *MNRAS*, 310, 1147
- Moustakas, L. A. & Metcalf, R. B. 2003, *MNRAS*, 339, 607
- Nemiroff, R. J. 1988, *ApJ*, 335, 593
- Ostensen, R., Refsdal, S., Stabell, R., Teuber, J., Emanuelsen, P. I., Festin, L., Florentin-Nielsen, R., Gahm, G., et al. 1996, *A&A*, 309, 59
- Parry, I., Mackay, C., Johnson, R., McMahon, R., Dean, A., Ramaprakash, A., King, D., Pritchard, J., et al. 2000, in *Proceedings of SPIE*, Vol. 4008, 1193 – 1202
- Peterson, B. M. 1993, *PASP*, 105, 247
- Peterson, B. M. & Wandel, A. 1999, *ApJ*, 521, L95

- Refsdal, S. & Stabell, R. 1991, *A&A*, 250, 62
- . 1997, *A&A*, 325, 877
- Robinson, A., Vila-Vilaro, B., Axon, D. J., Perez, E., Wagner, S. J., Baum, S. A., Boisson, C., Durret, F., et al. 1994, *A&A*, 291, 351
- Savage, B. D., Drake, J. F., Budich, W., & Bohlin, R. C. 1977, *ApJ*, 216, 291
- Schmidt, R., Webster, R. L., & Lewis, G. F. 1998, *MNRAS*, 295, 488
- Schneider, P. & Wambsganss, J. 1990, *A&A*, 237, 42
- Somerville, R. S. 2002, *ApJ*, 572, L23
- Trott, C. M. & Webster, R. L. 2002, *MNRAS*, 334, 621
- Ulrich, M., Maraschi, L., & Urry, C. M. 1997, *ARA&A*, 35, 445
- Wambsganss, J., Schneider, P., & Paczynski, B. 1990, *ApJ*, 358, L33
- Wandel, A. 1999, *ApJ*, 527, 649
- Woźniak, P. R., Alard, C., Udalski, A., Szymański, M., Kubiak, M., Pietrzyński, G., & Zebruń, K. 2000, *ApJ*, 529, 88
- Wyithe, J. S. B., Agol, E., & Fluke, C. J. 2002, *MNRAS*, 331, 1041
- Wyithe, J. S. B., Webster, R. L., & Turner, E. L. 2000a, *MNRAS*, 318, 762
- Wyithe, J. S. B., Webster, R. L., Turner, E. L., & Mortlock, D. J. 2000b, *MNRAS*, 315, 62
- Yonehara, A. 2001, *ApJ*, 548, L127
- Zentner, A. R. & Bullock, J. S. 2003, *apJ* in press, astro-ph/0304292